

# A Method for Enforcing Integrability in Shape from Shading Algorithms

ROBERT T. FRANKOT, MEMBER, IEEE, AND RAMA CHELLAPPA, SENIOR MEMBER, IEEE

**Abstract**—Several recently developed techniques for reconstructing surface shape from shading information estimate surface slopes without ensuring that they are integrable. This paper presents an approach for enforcing integrability, a particular implementation of the approach, an example of its application to extending an existing shape-from-shading algorithm, and experimental results showing the improvement that results from enforcing integrability.

A possibly nonintegrable estimate of surface slopes is represented by a finite set of basis functions, and integrability is enforced by calculating the orthogonal projection onto a vector subspace spanning the set of integrable slopes. This projection maps closed convex sets into closed convex sets and, hence, is attractive as a constraint in iterative algorithms. The same technique is also useful for noniterative algorithms since it provides a least-squares fit of integrable slopes to nonintegrable slopes in one pass of the algorithm. The special case of Fourier basis functions is also formulated. This provides an intuitive frequency domain interpretation of shape from shading, a computationally efficient implementation using fast Fourier transforms, and a convenient method for introducing low-resolution information into the shape-from-shading solution. Reconstruction of surface height by integrating surface slope estimates is obtained as a byproduct of the integrability constraint.

The integrability projection constraint was applied to extending an iterative shape-from-shading algorithm of Brooks and Horn. Experimental results show that the extended algorithm converges faster and with less error than the original version. Good surface reconstructions were obtained with and without known boundary conditions and for fairly complicated surfaces. Simulation examples show that the algorithm is robust with respect to large (but known) changes in illumination geometry, obtaining high-quality reconstructions even in the presence of significant shadowing.

Other possible applications of this method to computer vision problems such as shape from texture and surface reconstruction from synthetic aperture radar imagery are discussed.

**Index Terms**—Computer vision, depth maps, integrability, photogrammetry, radarclinometry, shape from shading, surface reconstruction, 2 1/2-D models.

## I. INTRODUCTION

SHAPE from shading refers to the problem of determining the shape of a smooth surface given a single

Manuscript received November 5, 1986. Recommended for acceptance by W. E. L. Grimson. This work was supported in part by the Hughes Doctoral Fellowship Program and in part by the National Science Foundation under Grant DCI 84-51010 and matching funds from Hughes Aircraft Company, IBM, and AT&T.

R. T. Frankot is with the Hughes Aircraft Company, Radar Systems Group, El Segundo, CA, and the Department of Electrical Engineering—Systems, Signal and Image Processing Institute, University of Southern California, Los Angeles, CA 90089.

R. Chellappa is with the Department of Electrical Engineering—Systems, Signal and Image Processing Institute, University of Southern California, Los Angeles, CA 90089.

IEEE Log Number 8717391.

image of that surface. One way to infer surface variations given a single image is to model the observed image intensity in terms of the surface orientation and then use that relationship to solve for the surface slopes.

Let  $I(x, y)$  be the observed image intensity and  $z(x, y)$  be the unknown surface height above the  $(x, y)$  plane. The relationship between image intensity and surface slopes can be expressed in the following form [1]–[3]:

$$I(x, y) = \mathcal{R}(z_x, z_y, \beta, l, \rho) \quad (1)$$

where

$$z_x = \frac{\partial z}{\partial x}$$

and

$$z_y = \frac{\partial z}{\partial y}$$

are the surface slopes,  $\beta$  is the illumination direction vector,  $l$  is the vector from the surface to the camera, and  $\rho$  is the albedo or intrinsic reflectivity of the materials composing the surface. It is also convenient to make the following assumptions: 1) at any point  $(x_0, y_0)$ , the reflectance map  $\mathcal{R}$  is a function of the surface slopes and albedo only at  $(x_0, y_0)$ , i.e., multiple reflections are ignored; 2) the albedo  $\rho$  and the vectors  $\beta$  and  $l$  are known over the entire image; and 3)  $\mathcal{R}$  is spatially invariant. The imaging geometry is illustrated in Fig. 1.

It has been observed [3] that shape from shading can be expressed as a problem of solving a first-order nonlinear partial differential equation in  $x$  and  $y$ . In deriving iterative solutions to (1) by the calculus of variations, it appears to be much more straightforward to solve for surface orientation than to solve directly for  $z$  [4]. The question of consistency between  $z_x$  and  $z_y$  then arises. A reasonable consistency constraint to place on the surface slopes is that they be integrable, where integrability is defined by

$$z_{xy}(x, y) = z_{yx}(x, y) \quad (2)$$

for all  $(x, y)$  on the support of  $I$ . That is, they correspond to a surface with second partial derivatives independent of the order of differentiation. As a result, the surface height at any particular point is independent of the path of integration. This can also be thought of as a smoothness constraint since a surface with discontinuities violates (2). Horn and Brooks assert [4], as do we, that past

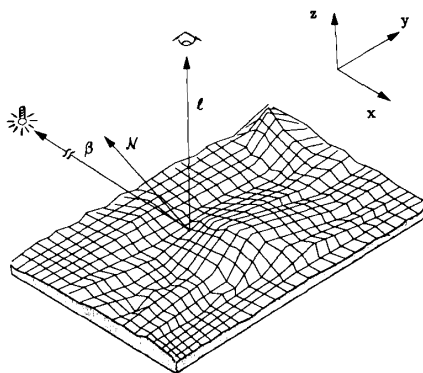


Fig. 1. Imaging geometry.

shape-from-shading algorithms can be improved considerably by incorporating such an integrability constraint.

Most shape-from-shading algorithms reported in the literature [5]–[10] do not take into account the interdependence of the two components of surface orientation, but allow them to vary independently. If we do allow  $(z_x, z_y)$  to vary independently, then (1) may have an infinite number of solutions even when boundary conditions are completely known and there are no modeling errors or observation noise. Just to illustrate this point, neglect the issue of boundary conditions and consider shape from shading as a discrete problem. Suppose we observe image intensity on an  $N \times N$  grid. We have  $N^2$  observations and hope to determine  $2N^2$  samples of the partial derivatives of  $z(x, y)$ . Clearly, there is an infinite number of solutions to (1) if the partial derivatives of  $z$  are not interdependent. Suppose instead that we simply require that these partial derivatives be integrable in the sense of (2). Then the partial derivatives must correspond to only  $N^2$  unknown samples of  $z$ , so that we are dealing with approximately  $N^2$  equations in  $N^2$  unknowns. Hence, an integrability constraint cuts the number of unknowns by a factor of two, neglecting boundary conditions.

Early solutions to the shape-from-shading problem were based on direct inversion of the differential equation (1) [1]–[3] and served to demonstrate the concept of shape from shading. Unfortunately, an exact solution to the imaging equation (1) does not always exist, or there may be an infinite number of solutions. In practice, modeling errors such as reflectance map mismatch, imperfect knowledge of the light source, spatial and radiometric quantization error, observation noise, and albedo variations are inevitable. Further, boundary conditions are generally not completely known and sometimes may not be available at all. These factors all influence the existence and uniqueness of a solution to (1) and the estimation of a good solution in the case that a unique one does not exist. For these reasons, shape from shading is a very difficult problem in practice.

It is more practical to pose shape from shading as a constrained minimization problem rather than purely an inversion problem. For example, Brooks and Horn [5]

proposed the approach of selecting the surface slope estimates  $(\hat{z}_x, \hat{z}_y)$  which minimize the following cost function:

$$\epsilon = \iint (I - \mathcal{R}(\hat{z}_x, \hat{z}_y))^2 + \lambda \cdot (\hat{z}_{xx}^2 + 2\hat{z}_{xy}^2 + \hat{z}_{yy}^2) dx dy, \quad (3)$$

subject to known boundary conditions. The first term in the integrand is the squared error between the observed image intensity and the image intensity predicted by substituting the estimates  $(\hat{z}_x, \hat{z}_y)$  into (1). This mean-squared error term allows for modeling errors and noise. The second term in the integrand is a measure of quadratic variation in the surface slopes. This is a smoothness criterion, which, in principle, assures a unique smooth solution to (3) even when (1) does not possess a unique solution. It is also interesting that minimization of a quadratic variation of the surface slopes is roughly equivalent to minimization of the potential energy of a thin elastic plate [11]. The constant  $\lambda$  establishes a tradeoff between the smoothness of the solution  $(\hat{z}_x, \hat{z}_y)$  and the mean-square value of the residuals  $I - \mathcal{R}$ .

Brooks and Horn [5] developed an algorithm to minimize  $\epsilon$  in (3), subject to the constraint that  $(\hat{z}_x, \hat{z}_y)$  satisfy known boundary conditions. Although the Brooks and Horn algorithm may converge to a unique solution of (3), that solution is generally not integrable. That is, given the final estimates of the partial derivatives, many possible surfaces could be constructed, each dependent on the path of integration.

Earlier, Ikeuchi and Horn [6] developed a similar algorithm that, instead of using gradient space  $(z_x, z_y)$ , was parameterized in stereographic coordinates  $(f, g)$  where

$$f = \frac{2z_x}{1 + \sqrt{1 + z_x^2 + z_y^2}}$$

and

$$g = \frac{2z_y}{1 + \sqrt{1 + z_x^2 + z_y^2}}. \quad (4)$$

This parameterization eliminates the difficulty in handling occluding boundaries where  $z_x$ ,  $z_y$ , or both are unbounded. To understand the  $(f, g)$  coordinates geometrically, note that the locus of all conceivable unit normal vectors defines a unit sphere, called the Gaussian sphere. The  $(f, g)$  coordinate system above can be obtained through a central projection from the south pole of the entire Gaussian sphere into a plane tangent at its north pole. The locus of all occluding boundaries corresponds to the equator of the Gaussian sphere and a circle of radius 2 in  $(f, g)$  space. The algorithm of Ikeuchi and Horn allows  $f$  and  $g$  to vary independently in the iterative solution, and  $(z_x, z_y)$  is obtained by a point transformation of  $(f, g)$ . The result is that Ikeuchi and Horn's algorithm also suffers from the drawback of not producing an integrable solution.

Lee [8] presented a shape-from-shading algorithm inspired by that of Ikeuchi and Horn, for which he proves the existence of a unique solution. Further, Lee proves that his algorithm converges to the unique solution if the surface slopes are known on the square image boundary. Unfortunately, that solution is not integrable.

Pentland [9] developed a technique which examines local estimates of the Laplacian of image intensity under the assumption that the surface is locally spherical at each point. Lee and Rosenfeld [7] later improved this technique so that it requires only first derivatives of image intensity, thereby reducing sensitivity to noise. Two difficulties with this local approach are the local sphericity assumption and the reliance on intensity derivatives, which can be very noisy. A third difficulty is that no provision is made for enforcing global consistency (e.g., integrability) of the local slopes, so that it is difficult to construct a surface from the slope estimates.

Integrability constraints have been used before in iterative shape-from-shading algorithms. Smith [12] derived a set of equations relating derivatives of image intensity to surface orientation independent of albedo and illumination angle and without assuming a particular local characteristic for the surface (such as Pentland's local sphericity assumption). It is illuminating to note that integrability was assumed in the formulation and imposed in deriving algorithms for solving the equations. Smith considered the use of a penalty function to encourage integrability during iteration and a local spatial approach for constructing a surface from nonintegrable slope estimates, although no convergent algorithm was reported.

Recently, Horn and Brooks [4] have developed an approach for deriving iterative shape-from-shading algorithms. In that paper are examples of iterative algorithms which do attempt to enforce integrability through the use of a penalty function. This represents a significant advance. However, Horn and Brooks encountered some difficulties in developing a convergent iterative algorithm that strictly enforces integrability. Further, the algorithms that were presented do not appear to allow much flexibility for incorporating additional constraints.

In this paper, we present a technique for strictly en-

forcing integrability, as in (2). The method for enforcing integrability is to project the possibly nonintegrable surface slope estimates onto the nearest integrable surface slopes [13]. In Section II, this orthogonal projection is solved for the case in which the surface slopes are represented by finite sets of orthogonal integrable basis functions. It is shown that the projection maps closed convex subsets of the space of nonintegrable surface slopes onto closed convex subsets of the space of integrable surface slopes, provided that certain conditions are met. Ikeuchi and Horn have previously derived an iterative algorithm, described in [4], that constructs depth information from nonintegrable surface orientation data by iteratively solving the same projection. That approach has the advantage of not requiring a finite basis function representation. Our method has the advantage of being noniterative along with all of the advantages and disadvantages of the basis function representation. In Section III, the projection is presented for the special case of Fourier basis functions. In Section IV, the discrete periodic Fourier basis formulation of the projection is applied to extending a shape-from-shading algorithm of Brooks and Horn [5] so that it converges faster and with much less error than the original version. Simulation results are presented for images of complicated surfaces representative of natural terrain. The technique is appropriate for integrating noisy slope estimates and could, perhaps, be used in improving the results of several other shape-from-shading algorithms [7]–[10], [12]. Finally, in Section VI, possible applications to shape from texture [10], [14], shape from synthetic aperture radar (SAR) imagery [23], and shape from coherent image amplitude [15] are discussed briefly.

## II. ENFORCING INTEGRABILITY BY ORTHOGONAL PROJECTIONS

There are many conceivable ways of enforcing (2). The key is to develop a computationally efficient method suitable for use with iterative algorithms. We have developed an approach based on projecting the possibly nonintegrable estimated surface slopes  $(\hat{z}_x, \hat{z}_y)$  onto a set of integrable surface slopes  $(\bar{z}_x, \bar{z}_y)$  where

$$\frac{\partial}{\partial y} \bar{z}_x = \frac{\partial}{\partial x} \bar{z}_y \quad (5)$$

while simultaneously minimizing the following distance measure:

$$d\{(\hat{z}_x, \hat{z}_y), (\bar{z}_x, \bar{z}_y)\} \\ = \iint |\bar{z}_x - \hat{z}_x|^2 + |\bar{z}_y - \hat{z}_y|^2 dx dy. \quad (6)$$

Note that the minimum distance property makes this an orthogonal projection.

The task of finding such a projection is simplified if we can represent the surface slopes by a finite set of integrable basis functions, each satisfying (5). Suppose that we represent the surface  $z(x, y)$  by the functions  $\phi(x, y)$ ,

$\omega$ ) so that

$$z(x, y) = \sum_{\omega \in \Omega} C(\omega) \phi(x, y, \omega) \quad (7)$$

where  $\omega = (\omega_x, \omega_y)$  is a two-dimensional index,  $\Omega$  is a finite set of indexes, and the members of  $\{\phi(x, y, \omega)\}$  are not necessarily mutually orthogonal. If each  $\phi(\omega)$  satisfies (5), then it follows that  $z$  does also. Note that the partial derivatives of  $z$  can also be expressed in terms of this expansion, giving

$$z_x(x, y) = \sum_{\omega \in \Omega} C(\omega) \phi_x(x, y, \omega)$$

and

$$z_y(x, y) = \sum_{\omega \in \Omega} C(\omega) \phi_y(x, y, \omega) \quad (8)$$

where  $\phi_x = (\partial\phi/\partial x)$  and  $\phi_y = (\partial\phi/\partial y)$ .

Now a method is presented for finding the expansion coefficients  $C(\omega)$  which minimize (6). Suppose that the members of  $\{\phi_x(x, y, \omega)\}$  as well as the members of  $\{\phi_y(x, y, \omega)\}$  are mutually orthogonal. Then we can compute the coefficients for the expansions of  $\hat{z}_x$  and  $\hat{z}_y$  such that

$$\hat{z}_x(x, y) = \sum_{\omega \in \Omega} \hat{C}_1(\omega) \phi_x(x, y, \omega)$$

and

$$\hat{z}_y(x, y) = \sum_{\omega \in \Omega} \hat{C}_2(\omega) \phi_y(x, y, \omega). \quad (9)$$

The orthogonality of the basis functions in (9) greatly simplifies the minimization of (6).

*Proposition 1:* The expansion coefficients  $\tilde{C}(\omega)$  in (7) that minimize (6) given a possibly nonintegrable estimate of surface slopes  $\hat{z}_x(x, y)$ ,  $\hat{z}_y(x, y)$  are given by

$$\tilde{C}(\omega) = \frac{P_x(\omega) \hat{C}_1(\omega) + P_y(\omega) \hat{C}_2(\omega)}{P_x(\omega) + P_y(\omega)} \quad (10)$$

for each  $\omega \in \Omega$  where  $P_x(\omega) = \iint |\phi_x(x, y, \omega)|^2 dx dy$  and  $P_y(\omega) = \iint |\phi_y(x, y, \omega)|^2 dx dy$ . The integrated surface  $\tilde{z}(x, y)$  and integrable surface slopes,  $\tilde{z}_x(x, y)$ ,  $\tilde{z}_y(x, y)$  are then obtained by substituting  $\tilde{C}(\omega)$  into the expansions (7) and (8).

*Proof:* By substituting the expansion for  $\hat{z}_x$ ,  $\hat{z}_y$ ,  $\tilde{z}_x$ , and  $\tilde{z}_y$  into (6), the distance measure becomes

$$\begin{aligned} d\{(\hat{z}_x, \hat{z}_y), (\tilde{z}_x, \tilde{z}_y)\} \\ = \iint \left| \sum_{\omega \in \Omega} \tilde{C} \phi_x - \sum_{\omega \in \Omega} \hat{C}_1 \phi_x \right|^2 \\ + \left| \sum_{\omega \in \Omega} \tilde{C} \phi_y - \sum_{\omega \in \Omega} \hat{C}_2 \phi_y \right|^2 dx dy, \quad (11) \end{aligned}$$

which reduces to

$$\begin{aligned} d\{(\hat{z}_x, \hat{z}_y), (\tilde{z}_x, \tilde{z}_y)\} = \iint \sum_{\omega \in \Omega} |\tilde{C} - \hat{C}_1|^2 |\phi_x|^2 \\ + \sum_{\omega \in \Omega} |\tilde{C} - \hat{C}_2|^2 |\phi_y|^2 dx dy \end{aligned}$$

because of the orthogonality of  $\{\phi_x(\omega), \omega \in \Omega\}$  and of  $\{\phi_y(\omega), \omega \in \Omega\}$ . By interchanging the order of summation and integration, the distance in (6) reduces to

$$\begin{aligned} d\{(\hat{z}_x, \hat{z}_y), (\tilde{z}_x, \tilde{z}_y)\} \\ = \sum_{\omega \in \Omega} |\tilde{C}(\omega) - \hat{C}_1(\omega)|^2 P_x(\omega) \\ + |\tilde{C}(\omega) - \hat{C}_2(\omega)|^2 P_y(\omega). \quad (12) \end{aligned}$$

Equation (12) can be minimized by minimizing each term of the summation individually. By differentiating (12) with respect to the real and imaginary parts of  $\tilde{C}(\omega)$  for each  $\omega$ , setting the result to zero and solving for  $\tilde{C}$ , (10) results.

For clarity in the subsequent proofs, express (8) and (9) in terms of vectors. First, define the vectors

$$\begin{aligned} \Phi_x(x, y) &= \text{col} [\phi_x(x, y, \omega), \omega \in \Omega] \\ \Phi_y(x, y) &= \text{col} [\phi_y(x, y, \omega), \omega \in \Omega] \\ \theta &= [0, \dots, 0] \\ \mathbf{C} &= \text{col} [\tilde{C}(\omega), \omega \in \Omega] \\ \mathbf{C}_1 &= \text{col} [\hat{C}_1(\omega), \omega \in \Omega] \\ \mathbf{C}_2 &= \text{col} [\hat{C}_2(\omega), \omega \in \Omega]. \end{aligned}$$

Equation (9) can now be written as

$$\begin{bmatrix} \hat{z}_x \\ \hat{z}_y \end{bmatrix} = \begin{bmatrix} \Phi_x^T & \theta \\ \theta & \Phi_y^T \end{bmatrix} \begin{bmatrix} \mathbf{C}_1 \\ \mathbf{C}_2 \end{bmatrix}, \quad (13)$$

with the set of possibly nonintegrable surface slopes expressed as

$$\mathcal{S}_0 = \text{span} \begin{bmatrix} \Phi_x^T & \theta \\ \theta & \Phi_y^T \end{bmatrix}. \quad (14)$$

Similarly, (8) can be rewritten as

$$\begin{bmatrix} \tilde{z}_x \\ \tilde{z}_y \end{bmatrix} = \begin{bmatrix} \Phi_x^T \\ \Phi_y^T \end{bmatrix} \mathbf{C}, \quad (15)$$

with the set of integrable surface slopes given by

$$\mathcal{S} = \text{span} \begin{bmatrix} \Phi_x^T \\ \Phi_y^T \end{bmatrix}, \quad (16)$$

which is a vector subspace of  $\mathcal{S}_0$ .

We will denote the mapping of  $\mathcal{S}_0$  onto  $\mathcal{S}$  using (10) as  $\mathcal{P}$ . This can be written in vector form as

$$\mathbf{C} = [\mathbf{P} \quad \mathbf{I} - \mathbf{P}] \begin{bmatrix} \mathbf{C}_1 \\ \mathbf{C}_2 \end{bmatrix} \quad (17)$$

where  $\mathbf{P}$  is a diagonal matrix with diagonal elements  $P_x/(P_x + P_y)$  and  $\mathbf{I}$  is the identity matrix.

*Proposition 2:* The projection (10) maps convex subsets of  $\{\hat{z}_x, \hat{z}_y\}$  onto convex subsets of  $\{\tilde{z}_x, \tilde{z}_y\}$ .

*Proof:* Convexity follows directly from the observation that (17) is a linear mapping. Suppose that  $\mathcal{E}$  is a convex subset of  $\mathcal{S}_0$ . Then  $\mathcal{P}(\mathcal{E})$  is a subset of  $\mathcal{S}$ , and we

must now prove that  $\mathcal{P}(\mathcal{E})$  is convex. The definition of convexity is that, for all  $\mathbf{U}, \mathbf{V} \in \mathcal{E}$  and for all  $0 < \mu < 1$ , we have  $\mu\mathbf{U} + (1 - \mu)\mathbf{V} \in \mathcal{E}$ . Then  $\mathcal{P}(\mu\mathbf{U} + (1 - \mu)\mathbf{V}) \in \mathcal{P}(\mathcal{E})$  since  $\mathcal{E}$  is convex.  $\mathcal{P}$  is linear so that

$$\begin{aligned} \mathcal{P}(\mu\mathbf{U} + (1 - \mu)\mathbf{V}) \\ = \mu\mathcal{P}(\mathbf{U}) + (1 - \mu)\mathcal{P}(\mathbf{V}). \end{aligned} \quad (18)$$

This proves that the right-hand side of (18) is an element of  $\mathcal{S}$ , thus completing the proof.

**Proposition 3:** The projection (10) maps compact subsets of the functions  $\{\hat{z}_x, \hat{z}_y\}$  onto compact subsets of  $\{\tilde{z}_x, \tilde{z}_y\}$ . Since we are working in metric spaces, this is equivalent to saying that closed and bounded sets are mapped onto closed and bounded sets [16].

*Proof:* From [16, theorem 4.15] we know that Proposition 3 holds if  $\mathcal{P}$  is a continuous mapping. Since all of the elements of the transformation in (17) are finite, it follows that  $\mathcal{P}$  is continuous, completing the proof.

It was shown that the integrability constraint represents an orthogonal projection mapping closed convex subsets of its input space onto closed convex subsets of its output space. This is a highly desirable property if the projection is to be applied as a constraint in iterative algorithms [17], [18]. The shape-from-shading problem, in its entirety, does not appear to lend itself well to solution by the method of projection onto convex sets (POCS) since the nonlinearity of the reflectance map makes it difficult to realize an orthogonal projection. However, it is possible to introduce additional constraints, e.g., integrability, into an iterative shape-from-shading algorithm using POCS as an intermediate step. An example of this is presented in Section IV. Note that the methods for enforcing boundary conditions in previous shape-from-shading algorithms [4]–[6], [8] could be expressed as projections onto closed convex sets. This follows from the fact that the operation of setting a function equal to prescribed values over some region of its support (e.g., strictly enforcing boundary conditions) can be expressed as an orthogonal projection mapping closed convex sets onto closed convex sets [17].

This approach for enforcing integrability has a second distinct advantage in that the surface can be reconstructed in one pass using all of the information available in  $(\hat{z}_x, \hat{z}_y)$  simply by performing the summation in (7) for the values of  $\tilde{C}(\omega)$  computed in (10). Thus, it may be useful as a more efficient integrator for nonrecursive local shape-from-shading approaches.

### III. INTEGRATION BY FOURIER EXPANSION

The usefulness of the expansion presented in Section II depends on the specific choice of basis functions. The Fourier basis functions  $\phi(x, y, \omega) = \exp(j\omega_x x + j\omega_y y)$  are particularly convenient computationally, and they also form a complete orthonormal basis for  $z$ .

Using this basis, the surface is represented by

$$z(x, y) = \sum_{\omega \in \Omega} \tilde{C}(\omega) \exp\{j\omega \cdot (x, y)\} \quad (19)$$

where  $\{\tilde{C}\}$  are the coefficients of the Fourier series expansion of  $\tilde{z}$ . For images of size  $N \times N$ , a reasonable choice for  $\Omega$  would be  $(2\pi n, 2\pi m)$ , with  $n, m \in \{0, 1, \dots, N - 1\}$ . Now let  $\hat{C}_x, \hat{C}_y, \tilde{C}_x, \tilde{C}_y$  be the Fourier coefficients for  $\hat{z}_x, \hat{z}_y, \tilde{z}_x, \tilde{z}_y$ , respectively.

The derivatives of the Fourier basis functions possess the following useful properties

$$\phi_x = j\omega_x \phi$$

and

$$\phi_y = j\omega_y \phi, \quad (20)$$

$P_x \propto \omega_x^2, P_y \propto \omega_y^2, \hat{C}_1(\omega) = \hat{C}_x(\omega)/j\omega_x$ , and  $\hat{C}_2(\omega) = \hat{C}_y(\omega)/j\omega_y$ . Then using (10) and (20), it is straightforward to show that (6) is minimized by taking

$$\tilde{C}(\omega) = \frac{-j\omega_x \hat{C}_x(\omega) - j\omega_y \hat{C}_y(\omega)}{\omega_x^2 + \omega_y^2}, \quad (21)$$

with the Fourier coefficients of the constrained surface slopes given by [13]

$$\tilde{C}_x(\omega) = j\omega_x \tilde{C}(\omega)$$

and

$$\tilde{C}_y(\omega) = j\omega_y \tilde{C}(\omega).$$

The expressions above are valid except at the point  $\omega = (0, 0)$ , which simply means that we cannot recover the average value of  $z$  without some additional information.

Note that

$$\omega_y \rightarrow 0 \Rightarrow \tilde{C}(\omega) \rightarrow \hat{C}_x(\omega)/j\omega_x$$

and

$$\omega_x \rightarrow 0 \Rightarrow \tilde{C}(\omega) \rightarrow \hat{C}_y(\omega)/j\omega_y.$$

In general, the Fourier coefficients of the raw slope estimates are combined in proportion to their relative frequencies. For example, if we divide the weight for  $\hat{C}_x(\omega)$  in (10) by that of  $\hat{C}_y(\omega)$ , we get  $\omega_x/\omega_y$ . The effect is to reduce ‘‘random walk’’ errors that result from amplification of low-frequency noise during integration.

This frequency domain interpretation helps in understanding an inherent difficulty in the shape-from-shading problem. The observed image intensity is a function of the derivatives of the surface. Equation (20) shows that the low-frequency information for the surface is lost in the image formation process. Hence, the reconstructed surface inevitably suffers from low-frequency distortion, the severity depending on observation noise characteristics. The frequency domain formulation of the integrability constraint is appropriate here since the low-resolution data could be introduced as a projection constraint in an iterative shape-from-shading algorithm. This is accomplished by substituting the Fourier coefficients of the low-resolution surface in place of the lowest-frequency shape-from-shading results. Experimental results in Fig. 6 of Section V demonstrate the improvement that results from

using four known low-frequency terms in compensating for completely unknown boundary conditions.

It is conceivable that low-resolution information could be drawn from other sources in real-world applications of shape-from-shading techniques. For example, in some remote sensing applications, low-resolution surface height information is available from digital terrain models (DTM's) [19], [20]. A particular example where low-resolution constraints on shape from shading is available and useful is the Magellan project's Venus Radar Mapper, which will collect SAR imagery of the surface of Venus along with much lower-resolution radar altimetry data [22]. With shape-from-shading techniques, it may be possible to improve on the resolution of the radar altimetry data by combining it with the higher-resolution SAR imagery.

#### A. Discrete Periodic Formulation

For computer implementation, some form of discretization is necessary. We have assumed, for computational simplicity, that the surface slopes are circularly periodic and evaluate the Fourier coefficients  $\hat{C}_x$  and  $\hat{C}_y$  using the discrete Fourier transform (DFT). With this discrete periodic formulation, (6) is minimized by

$$\tilde{C}(\omega) = \frac{a_x^*(\omega_x) \hat{C}_x(\omega) + a_y^*(\omega_y) \hat{C}_y(\omega)}{|a_x|^2 + |a_y|^2} \quad (22)$$

with

$$\tilde{C}_x(\omega) = a_x(\omega_x) \tilde{C}(\omega)$$

and

$$\tilde{C}_y(\omega) = a_y(\omega_y) \tilde{C}(\omega)$$

where  $a_x$  and  $a_y$  are the Fourier coefficients of the appropriate discrete differentiation operator in  $x$  and  $y$ . Suppose we approximate the derivatives by finite central differences, e.g.,

$$z_y(l, m) \approx \frac{1}{2}[z(l+1, m) - z(l-1, m)] \quad (23)$$

and similarly for  $z_x$ . For the central difference operator above, we get  $a_y(\omega_y) = (1/2) \exp\{j\omega_y\} - (1/2) \exp\{-j\omega_y\} = j \sin(\omega_y)$ , and similarly,  $a_x(\omega_x) = (1/2) \exp\{j\omega_x\} - (1/2) \exp\{-j\omega_x\} = j \sin(\omega_x)$ .

The estimated surface is constructed by performing the inverse DFT of  $\tilde{C}(\omega)$  from (22), so that the integrability projection doubles as an integrator. In all cases, the DFT is evaluated using a fast Fourier transform (FFT) algorithm. The intuitive frequency domain interpretation of the integrability projection is easily extended to the discrete case using the discrete periodic formulation.

Alternatives to the discrete periodic formulation are possible, but are not considered in this paper. The Fourier expansion could be formulated on a finite lattice instead of a periodic lattice. The mathematics are somewhat more complicated, but FFT calculations are still possible [21], and more careful attention could then be paid to boundary

conditions. Other basis functions, such as Chebyshev polynomials, could also be useful for finite lattice realizations.

#### IV. AN IMPROVED SHAPE-FROM-SHADING ALGORITHM

We have utilized the projection from Section III to obtain a simple extension of an algorithm presented by Brooks and Horn [5]. The result is an algorithm which minimizes (3) while satisfying the discrete form of (5) and (6) at each iteration. The experimental results presented in Section V show a marked improvement in performance due to the integrability constraint.

Using the finite difference approximations, the values of  $\hat{z}_x(x, y)$  and  $\hat{z}_y(x, y)$  which minimize (3) are found iteratively by the following recursion for each point  $(x, y)$ :

$$\begin{bmatrix} \hat{z}_x \\ \hat{z}_y \end{bmatrix}_{k+1} = \begin{bmatrix} \hat{z}_x \\ \hat{z}_y \end{bmatrix}_k + \lambda_1(I - \mathcal{R}) \begin{bmatrix} \mathcal{R}_x \\ \mathcal{R}_y \end{bmatrix} \quad (24)$$

at the  $(k+1)$ th iteration where

$$\mathcal{R}_x = \frac{\partial \mathcal{R}}{\partial z_x}$$

and

$$\mathcal{R}_y = \frac{\partial \mathcal{R}}{\partial z_y}$$

$\mathcal{R}$  and its partials are evaluated at  $[\hat{z}_x, \hat{z}_y]_k$ ,  $\lambda_1$  is a constant inversely proportional to  $\lambda$  in (3),  $[\hat{z}_x, \hat{z}_y]_k$  is a smoothed version of  $[\bar{z}_x, \bar{z}_y]_k$ , and  $[\bar{z}_x, \bar{z}_y]_k$  is obtained by substituting the raw estimates  $[z_x, z_y]_k$  into the integrability projection (22).

The smoothing applied during each iteration is given by [5]

$$\begin{aligned} \hat{z}_y(l, m) = & \frac{1}{5}[\bar{z}_y(l, m+1) + \bar{z}_y(l, m-1) \\ & + \bar{z}_y(l+1, m) + \bar{z}_y(l-1, m)] \\ & + \frac{1}{20}[\bar{z}_y(l-1, m-1) \\ & + \bar{z}_y(l-1, m+1) \\ & + \bar{z}_y(l+1, m+1) + \bar{z}_y(l+1, m-1)] \end{aligned} \quad (25)$$

and similarly for  $\hat{z}_x$ . Note that this is just a discrete approximation to the Laplacian with the center pixel left out. This follows from a manipulation of a discrete form of the Euler equations for (3) as discussed in [4], [5]. The rationale for evaluating  $\mathcal{R}$  with the smoothed slope estimates is that it stabilizes (24) [6].

The iterative algorithm can be summarized as follows [13]:

- 1) Smooth the previous slope estimates using (25),
- 2) generate a new set of raw slope estimates using (24), and

3) project the raw slope estimates onto the nearest integrable solution using (22).

The process is repeated until the cost function either stops decreasing or becomes sufficiently small. The surface height is obtained by simply performing the inverse DFT of  $\tilde{C}(\omega)$  after the final iteration.

Parameterization in gradient space  $(z_x, z_y)$  rather than stereographic coordinates  $(f, g)$  is sometimes criticized because the surface gradient is not well defined at occluding boundaries where  $z_x, z_y$ , or both are infinite. However, for discrete data,  $z_x$  and  $z_y$  are bounded for all practical purposes. This observation leads to a potential method for utilizing occluding boundaries in the above shape-from-shading algorithm. Intuitively, it seems that most of the information provided by the occluding boundary comes from knowledge of the location of its contour in the  $(x, y)$  plane and the orientation  $z_x/z_y$  along its contour. The occluding boundary can be detected by examining zero crossings of the Laplacian of image intensity [11]. The orientation of the occluding boundary  $z_x/z_y$  can be found from analysis of this occluding contour. Then, perhaps, the orientation can be enforced as a constraint in the shape-from-shading solution while allowing the magnitude  $\sqrt{z_x^2 + z_y^2}$  to be controlled by the regularization penalty in (3). Alternatively, it is possible to apply the integrability constraint in gradient space and the surface slope update in  $(f, g)$  coordinates.

## V. EXPERIMENTAL RESULTS

The above algorithm was tested on synthetic imagery with and without known boundary conditions and was also tested on real imagery. In each case discussed below, the images are of size  $64 \times 64$  pixels. Lambertian surfaces illuminated by point sources were assumed in each case, giving the following the reflectance map:

$$\mathcal{R}(z_x, z_y, \beta, l, \rho) = \rho \frac{\beta_x z_x + \beta_y z_y + \beta_z}{\sqrt{\beta_x^2 + \beta_y^2 + \beta_z^2} \sqrt{1 + z_x^2 + z_y^2}}. \quad (26)$$

However, the implemented algorithm used numerical derivatives of the reflectance map, so that any reasonably well-behaved known reflectance map could have been applied.

### A. Comparison of Constrained Versus Unconstrained Algorithm

First, a series of experiments was performed to compare the performance of the shape-from-shading algorithm in Section IV with and without the integrability constraint. An image was simulated for a surface consisting of a partial sphere protruding above a plane.

In the first experiment, the surface slopes were provided where the sphere intersects the plane. No noise was added to the observed intensity, the only source of errors being intensity quantization and finite precision arithmetic. Under these conditions, the algorithm of Brooks and

Horn converges to a reasonably accurate solution for the surface slopes. This case was used to get an indication of the impact of enforcing the integrability projection under very benign conditions. Table I shows the mean and standard deviations of the surface orientation error for both the constrained and unconstrained algorithm after 100 iterations. Note that the application of the integrability constraint reduces the error standard deviation from  $2.36$  to  $0.53^\circ$ , a factor of 4.5. A second observation is that a minimum value of  $\lambda = 7000$  was required for stabilizing the unconstrained algorithm, whereas the constrained algorithm was stable for a wider range, down to  $\lambda = 5000$ . Interestingly, the very significant change in  $\lambda$  (from 7000 to 5000) resulted in an insignificant change in the error standard deviation (from 0.53 to 0.56), perhaps indicating that most of the smoothing is coming from the integrability constraint. This appears to corroborate the finding of Horn and Brooks [4] where the regularization penalty from (3) was dropped and an integrability penalty was used instead, improving on the results of Ikeuchi and Horn [6].

The rate of convergence was also compared for the partial sphere case. For the constrained algorithm, the orientation error standard deviation was down to  $2.7^\circ$  after only five iterations. The unconstrained algorithm took about 90 iterations to reach this same level of convergence. After eight iterations, the constrained algorithm was down to  $1.25^\circ$  error standard deviation, whereas the unconstrained algorithm took nearly 1000 iterations to reach the same level. This demonstrates that enforcing integrability by the method developed in this paper can greatly speed up convergence.

Similar experiments were repeated with relaxed boundary conditions, i.e., boundary conditions provided around the square border of the image. The integrability constraint also reduced the error standard deviation by a factor of about 4.5 in this case. The numerical comparison is shown in Table II.

When the unconstrained algorithm was applied with relaxed boundary conditions, the resulting solution was nearly locally cylindrical (i.e.,  $\hat{z}_y \approx 0$ ) everywhere. This is clearly nonintegrable. The integrability projection was applied to the above erroneous slope estimates after 100 iterations of the unconstrained algorithm. Here, the error standard deviation is much higher than for constrained iteration, but significantly lower than for unconstrained iteration, as indicated in Table II. This demonstrates the usefulness of the integrability projection as a method for constructing a surface from nonintegrable slope estimates.

Fig. 2(a) shows the true partial sphere surface; Fig. 2(b) shows an image generated from that surface; Fig. 2(c) shows the surface estimated using the constrained algorithm given both the image intensity and knowledge of the surface slopes around the border of the image (corresponding to Table II); and Fig. 2(d) shows the surface estimated given only the simulated image without knowledge of boundary conditions. For the known boundary condition case, the reconstructed surface is almost iden-

TABLE I  
COMPARISON OF SURFACE ORIENTATION ERROR AFTER 100 ITERATIONS FOR  
THE UNCONSTRAINED ALGORITHM VERSUS THE CONSTRAINED ALGORITHM.  
THE BOUNDARY SLOPES ARE PROVIDED AT THE INTERSECTION OF THE  
SPHERE AND THE PLANE IN THESE EXAMPLES

Algorithm	$\lambda$	Orientation Error (Degrees)	
		mean	st. dev.
Unconstrained	7000	4.07	2.36
Constrained	7000	0.64	0.56
Constrained	5000	0.61	0.53

TABLE II  
COMPARISON OF SURFACE ORIENTATION ERROR AFTER 100 ITERATIONS FOR  
THE UNCONSTRAINED ALGORITHM VERSUS THE CONSTRAINED ALGORITHM.  
IN THESE EXAMPLES, BOUNDARY CONDITIONS ARE SUPPLIED AROUND THE  
SQUARE BORDER OF THE IMAGE

Algorithm	$\lambda$	Orientation Error (Degrees)	
		mean	st. dev.
Unconstrained	7000	6.49	10.33
Unconstrained (until last iteration)	7000	8.45	6.66
Constrained	5000	1.89	2.45

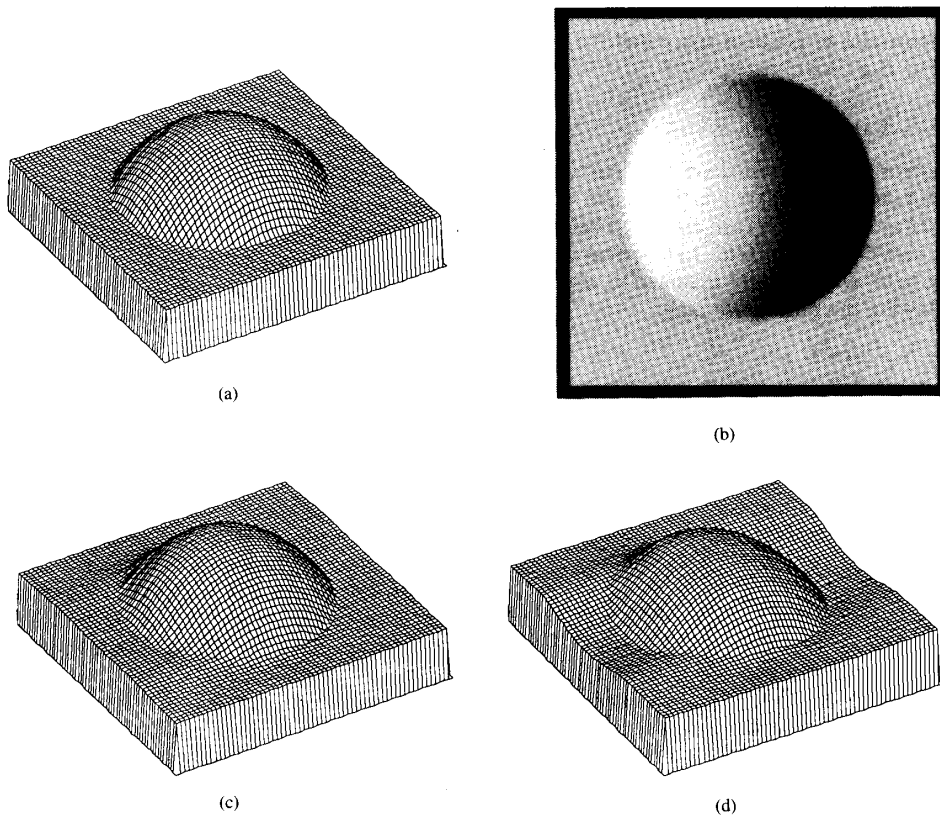


Fig. 2. Shape-from-shading results using simulated imagery. (a) The true surface shape. (b) An image simulated from the surface in (a). (c) The surface estimated by assuming that all surface slopes around the border of the image are zero, corresponding to Table II. (d) The surface estimated with unknown boundary slopes.

tical to the true surface. For the case of unknown boundary conditions, use of the regularization penalty term in (3) combined with the integrability constraint was sufficient to provide convergence to a reasonable solution in all test cases.

The positive results above can be attributed mostly to the integrability constraint, although other issues deserve some attention. Illumination from the side (instead of directly overhead) has a positive impact on the results. Had the sphere been illuminated from directly overhead, one would not be able to distinguish a concave-downward sphere from a concave-upward sphere using shading alone. Some other information would be needed, such as boundary slopes at the joint between the sphere and the plane or low-resolution surface information. This did not appear to be a very serious issue in our experiments since a slight deviation of the illumination source from vertical would allow the algorithm to resolve this type of ambiguity. No special measures were taken to avoid wrap-around due to the discrete periodic formulation of the integrability projection:  $N \times N$  FFT's were used for  $N \times N$  images. Similar methods have been used before in solving similar elliptic problems [21]. Periodicity appears to help a little bit for surfaces without discontinuities at the wraparound points, such as in Fig. 2, but it has a slight negative impact for more complicated surfaces.

### B. Shape-from-Shading for Complicated Surfaces

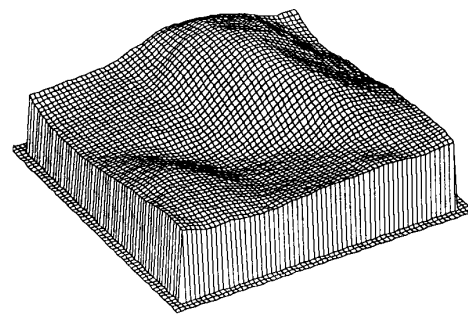
A second set of experiments demonstrates the performance of the constrained shape-from-shading algorithm using images of more complicated surfaces. In Fig. 3, a picture of the surface of the moon is shown along with a surface estimate based on a guessed light source direction and an assumed reflectance map. Boundary conditions are neither known nor guessed in advance, and a reasonable surface estimate is obtained. Although the lunar surface may be non-Lambertian [2], the surface estimate shown in Fig. 3 was obtained by assuming Lambertian reflectivity. For this moon image, surface estimates consistent with our visual intuition were obtained using a variety of assumed reflectance maps and for a broad range of plausible light source directions.

Images were simulated using a digital terrain model (DTM) of the Laguna Hills in California. Fig. 4 shows three-dimensional (3-D) plots of the true DTM and the results of the constrained shape-from-shading algorithm after 50 iterations. Comparison of the 3-D plot in Fig. 4(a) with those of Fig. 4(b) and (c) show that the general shape of the surface has been reconstructed both with and without known boundary conditions. The 1-D slices compared in Fig. 5 better illustrate how closely the reconstructed surface (dotted line) fits the true surface (solid line) in the known boundary conditions case.

The dashed line in Fig. 6 shows a 1-D slice of the surface reconstruction obtained with completely unknown boundary conditions. Although the overall shape of the reconstruction is very similar to that of the true surface (solid line), there is some apparent low-frequency distortion.



(a)



(b)

Fig. 3. Shape-from-shading results for real imagery of the moon. (a) The observed image. (b) The estimated surface.

This distortion is caused by the loss of low-frequency information in the process of image formation, combined with the tendency of the regularization penalty and periodic boundary conditions to flatten the surface. Qualitatively similar low-frequency errors appear in the solution for  $z(x, y)$  when small amounts of observation noise or other sources of error are present. This low-frequency distortion is an inherent part of the shape-from-shading problem since we are observing image intensity, which is a function of the partial derivatives of  $z(x, y)$ . The reconstruction of  $z(x, y)$  involves integrating those partial derivatives, amplifying the low-frequency portion of the noise spectrum, as discussed in Section III. Thus, it is important to be able to include low-frequency constraints from other sources.

### C. Incorporating Low-Resolution Information

The dotted line in Fig. 6 shows the improvement that results from including a very small amount of low-resolution data in the shape-from-shading solution. This demonstrates that if low-resolution information is indeed available in some form other than shading, then errors resulting from missing boundary conditions and observation noise can be greatly reduced. The application of the

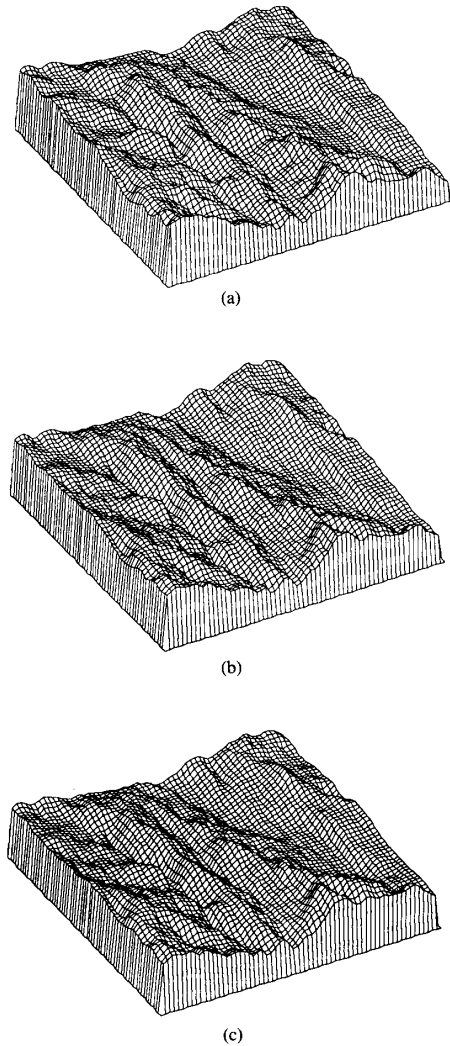


Fig. 4. (a) Laguna Hills DTM. (b) Estimated DTM obtained from a simulated image of the surface in (a) and known boundary slopes. (c) Estimated surface obtained with unknown boundary slopes.

integrability constraint lends itself well to including low-resolution information as a constraint in the iterative shape-from-shading algorithm of Section IV. This was accomplished by taking the Fourier transform of the Laguna DTM in Fig. 4, and saving only the four lowest-frequency terms (not including the dc term). The four lowest-frequency terms of the true DTM were then substituted for the corresponding part of the Fourier transform of the estimated surface height at each iteration. This did not add significantly to the computational load because the Fourier transform of estimated surface height is obtained as a byproduct of the integrability constraint, as can be seen from (21). Enforcing the low-frequency data as a projection constraint did not appear to slow down convergence in the cases tested

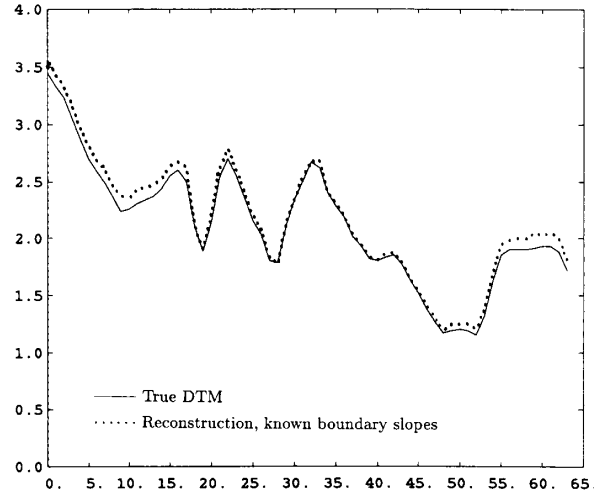


Fig. 5. One-dimensional slice through the DTM's of Fig. 4(a) and (b). The horizontal axis corresponds to the 32nd line in the images of Fig. 7. That is, it forms a line parallel to the  $x$  axis running from left to right through the center of the images. The units for the vertical axis are the same as the image sample spacing in  $(x, y)$ .

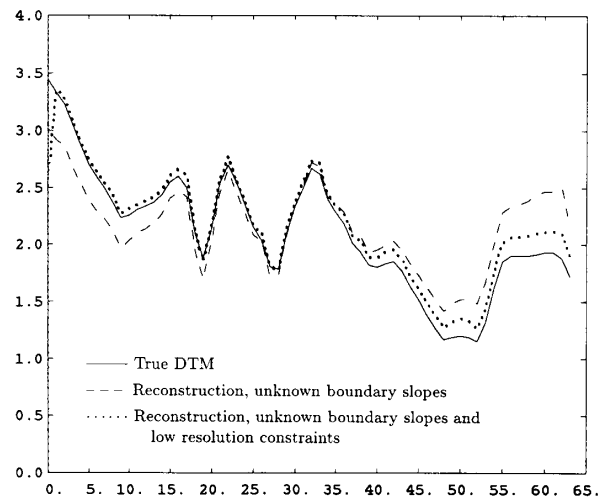


Fig. 6. One-dimensional slice comparing the true DTM, shape-from-shading results with unknown boundary conditions [Fig. 4(c)], and shape from shading with unknown boundary conditions, but utilizing low-frequency constraints provided by the 0.1 percent lowest-frequency Fourier coefficients of the true DTM.

#### D. Synthesis Results

The shape-from-shading algorithm was used to obtain a viewpoint-independent representation of the image suitable for predicting image intensity patterns. In Figs. 7 and 8, predicted images are synthesized for various illumination geometries given true surface shapes and also given surface slope estimates obtained using the constrained shape-from-shading algorithm of Section IV.

The top row of Fig. 7 shows simulated images for the partial sphere from Fig. 2 created with four different il-

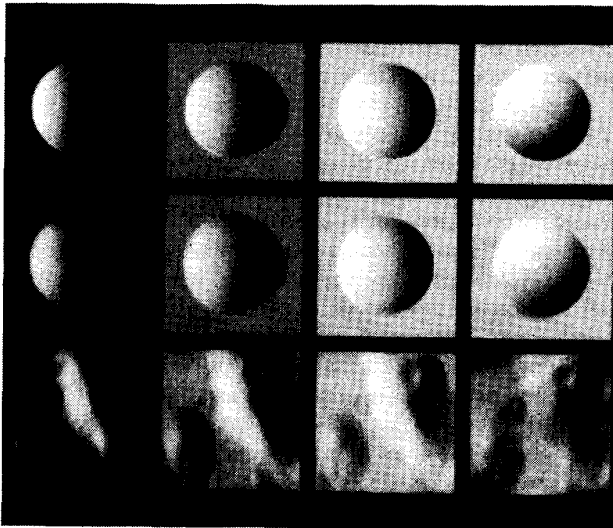


Fig. 7. Simulated images for various imaging geometries given shape-from-shading results. The first row shows the images simulated from the true partial sphere surface of Fig. 2. The second row uses the reconstructed surface given only the image intensity in Fig. 2, and the third row uses a surface estimated from the moon image of Fig. 3.

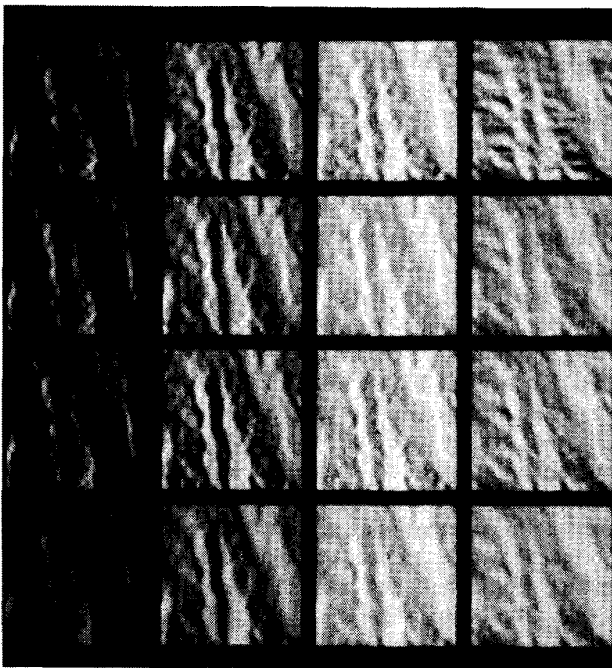


Fig. 8. Simulated images given true DTM compared to images predicted by shape-from-shading results. The first (top) row shows images simulated from the DTM for various illumination directions. The second row contains predicted images for those same illumination geometries, but using the surface estimate given the first image from row one. The third, fourth, and fifth rows use the surfaces estimated given the second, third, and fourth images, respectively, from row one.

illumination directions. The second row synthesizes images with the same four illumination directions, but using the surface reconstruction from Fig. 2(b), which uses known boundary conditions around the border of the im-

age. The close match between each of the images in the second row and their counterparts in the first row appears to indicate that the shape-from-shading algorithm is utilizing most of the information available in the observed image intensity. The third row uses the moon surface estimate from Fig. 3(b). Although ground truth is not available for testing the accuracy of this solution, it is encouraging that the surface estimate did produce a set of synthesized images that are consistent with our visual intuition.

Fig. 7 also reminds us that the human visual system does a good job of evaluating surface shape from image intensity for a wide variety of illumination conditions. Then it is reasonable to ask if the shape-from-shading algorithm can also produce high-quality surface reconstructions without much sensitivity to illumination geometry. In Fig. 4, simulated images created using four different illumination geometries were used to test the constrained shape-from-shading algorithm. First, simulated images were created using the DTM from Fig. 4, given the various illumination directions. This is shown in the top row. Second, the shape-from-shading algorithm was applied to each of those images. The resulting four surface slope estimates were each used to simulate four images using the same set of four illumination directions. These images are presented in the four subsequent rows. For example, the DTM was reconstructed given the first (leftmost) image in the top row, and that surface was used in simulating all of the images in the second row from the top. The surface reconstruction obtained from the second image in the top row was used in forming the four images in the third row, and so on. The purpose of forming the synthesized images is so that we can examine the sensitivity of the observables (image intensity) to errors in the function we want to estimate (surface shape) over a range of operating conditions (illumination geometry in this example).

Inspection of the images in Fig. 8 for constant illumination geometry, i.e., within the same column, shows very little difference in the synthesized images. The most notable difference is a slight smoothing in the direction orthogonal to the illumination vector  $\beta$ , as could be predicted by examining the partial derivatives of the reflectance map in (24). Fig. 8 demonstrates that the constrained shape-from-shading algorithm obtains results that are not sensitive to the illumination geometry of the observed image, provided that it is known. This indicates that the constrained shape-from-shading algorithm is robust with respect to illumination geometry.

Notice that a significant portion of the first image in Fig. 8 is covered by shadows. A reasonable surface estimate was still obtained, as indicated by the predicted images in the second row of Fig. 8. Fig. 9 shows a representative 1-D cut through the surface reconstructed from the shadowed image as compared to the true surface and a surface estimated from an image free from shadows. It is possible, in principle, to extract powerful surface orientation constraints at shadow entry points and the relative heights between shadow entry and exit points. How-

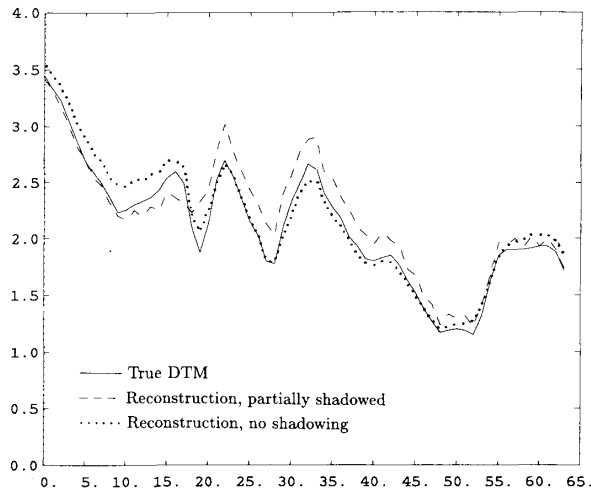


Fig. 9. One-dimensional slice showing true DTM and the estimated surface given a partially shadowed simulated image of the surface compared to an estimate made from an image without shadows. No attempt was made to utilize the relative height information available from the shadow boundaries.

ever, it can be difficult to detect shadows and locate their entry and exit points reliably. The predictive ability of even partial shape-from-shading results might provide a method of distinguishing between shadows and areas with very low albedo. Hence, we wanted to test the "robustness" of the shape-from-shading algorithm when confronted with shadowing, while not taking advantage of the constraints that are, in principle, available from shadowing. The only provision made in obtaining shape-from-shading results for partially shadowed images was to set  $\lambda_1 = 0$  in the shadowed regions. This is equivalent to setting the albedo to zero in shadows, in effect ignoring the nonexistent shading information and letting the regularization penalty and integrability projection bridge the gaps left by cast shadows. This worked well with small but significant degrees of shadowing. As shadowing becomes more severe, the algorithm becomes more difficult to stabilize.

## VI. DISCUSSION

The projection represented by (21) was used to provide a very effective extension to the iterative shape-from-shading algorithm of Brooks and Horn [5]. The resulting extension converged relatively well for a variety of test cases.

This technique also can be used as an integrator which minimizes the effects of local errors by combining all of the available information in a globally consistent manner. Accordingly, it may be useful for improving other computer vision techniques that obtain possibly erroneous local derivative estimates. Two obvious examples are the shape-from-texture work reported by Witkin [14] and the technique recently reported by Pentland [10] which attempts to unify shape from texture with shape from shad-

ing. In both papers, mention was made of difficulties encountered in reconstructing a depth map by integrating inexact surface orientation estimates.

Shape-from-shading results were presented in Section V demonstrating a case where, for all practical purposes, knowledge of the 0.1 percent lowest-frequency Fourier coefficients of the surface makes up for the fact that boundary conditions are completely unknown. This is exactly the situation in some remote sensing applications: boundary conditions are not available, but low-resolution information is. For example, the Magellan project will provide SAR imagery of the surface of Venus along with much lower resolution radar altimetry data [22]. The algorithm in Section IV easily combines the low-resolution altimetry data with high-resolution shading information. A simple extension such that the algorithm is suitable for SAR imagery is developed in [23]. Incidentally, a crude estimate of the reflectance map and large-scale albedo variations could be obtained by comparing the low-resolution altimetry data with the observed SAR image intensity.

A second application for the low-frequency constraint capability is in combining stereo information with shading information. Correspondence between stereo image pairs provides low-frequency information not available in shading alone. Conversely, shading provides information not available from either sparse or low-resolution stereo correspondences. Further, illumination differences between stereo image pairs (for photographs taken at different times of the day or for SAR imagery) may limit the accuracy of stereo image matching. It should be possible, therefore, to use shading and stereo information synergistically.

During the preparation of this paper, a recent paper was discovered [24] which uses a similar integrability constraint to unwrap the phase of complex SAR imagery in two dimensions. A fast least-squares approach was presented there which removes the inconsistencies in local phase derivative calculations (due to phase ambiguities and noise) to provide a phase image. What is most interesting here in the context of computer vision is that the phase of a coherent image (e.g., SAR) pixel is related to surface structure. Hence, phase may provide depth information not completely available from image intensity alone. The contribution of phase in determining surface structure is an underlying principle in some applications of speckle interferometry [25] and also was utilized for SAR imagery in one dimension by Harger [15]. It may be possible to combine phase and shading information for surface shape reconstruction. Interestingly, the technique presented in this paper is applicable to both components of that problem.

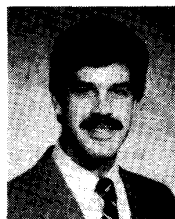
## ACKNOWLEDGMENT

The authors wish to thank T. Simchony and R. Leahy of the University of Southern California Signal and Image Processing Institute and the anonymous reviewers for sev-

eral insightful suggestions which improved the quality of this paper. They are indebted to R. Hudson, D. Evans, and R. Wojslaw of Hughes Aircraft Company for some enlightening discussions during the formative stages of this work. The first author would also like to thank S. Baumgarten and T. Jentes of Hughes Aircraft Company, whose continuing support as Department Managers helped to make this work possible.

## REFERENCES

- [1] J. Van Diggelen, "A photometric investigation of the slopes and heights of the ranges of hills in the Maria of the moon," *Bull. Astron. Inst. Netherlands*, vol. 11, July 1951.
- [2] T. Rindfleisch, "Photometric method for lunar topography," *Photogrammetric Eng.*, vol. 32, pp. 262-276, 1966.
- [3] B. K. P. Horn, "Obtaining shape from shading information," in *The Psychology of Machine Vision*, P. H. Winston, Ed. New York: McGraw-Hill, 1975, pp. 115-155.
- [4] B. K. P. Horn and M. J. Brooks, "The variational approach to shape from shading," *Comput. Vision Graphics Image Processing*, vol. 33, pp. 174-208, Feb. 1986.
- [5] M. J. Brooks and B. K. P. Horn, "Shape and source from shading," in *Proc. Int. Joint Conf. Artif. Intell.*, Los Angeles, CA, Aug. 1985, pp. 932-936.
- [6] K. Ikeuchi and B. K. P. Horn, "Numerical shape from shading and occluding boundaries," *Artif. Intell.*, vol. 17, pp. 141-184, 1981.
- [7] C. H. Lee and A. Rosenfeld, "Improved methods of estimating shape from shading using light source coordinate system," *Artif. Intell.*, vol. 26, pp. 125-143, 1985.
- [8] D. Lee, "A provably convergent algorithm for shape from shading," presented at the DARPA Image Understanding Workshop, Miami Beach, FL, Dec. 1985, pp. 489-496.
- [9] A. P. Pentland, "The Visual Inference of Shape: Computation From Local Features," Ph.D. dissertation, Dep. Psychology, M.I.T., Cambridge, MA, 1982.
- [10] —, "Shading into texture," *Artif. Intell.*, vol. 29, pp. 147-170, Aug. 1986.
- [11] W. E. L. Grimson, *From Images to Surfaces*. Cambridge, MA: M.I.T. Press, 1981.
- [12] G. B. Smith, "The relationship between image irradiance and surface orientation," presented at the IEEE Conf. Comput. Vision Pattern Recognition, Washington, DC, June 1983.
- [13] R. T. Frankot and R. Chellappa, "An improved algorithm for the shape from shading problem," in *Proc. Indian Inst. Sci. Conf. Syst. Signal Processing*, Bangalore, India, Dec. 11-13, 1986.
- [14] A. P. Witkin, "Recovering surface shape and orientation from texture," *Artif. Intell.*, vol. 17, pp. 17-46, 1981.
- [15] R. O. Harger, "Sea surface height estimator using synthetic aperture radar complex imagery," *IEEE J. Oceanic Eng.*, vol. OE-8, pp. 71-78, Apr. 1983.
- [16] W. Rudin, *Principles of Mathematical Analysis*, 3rd ed. New York: McGraw-Hill, 1976.
- [17] D. C. Youla and H. Webb, "Image restoration by the method of convex projections: Part I—Theory," *IEEE Trans. Med. Imaging*, vol. MI-1, pp. 81-94, Oct. 1982.
- [18] H. J. Trussell and M. Civanlar, "The feasible solution in signal restoration," *IEEE Trans. Acoust., Speech, Signal Processing*, vol. ASSP-32, pp. 201-212, Apr. 1984.
- [19] B. K. P. Horn and B. L. Bachman, "Using synthetic images to register real images with surface models," *Commun. ACM*, vol. 21, pp. 914-924, Nov. 1978.
- [20] R. J. Woodham, "Using digital terrain data to model image formation in remote sensing," *Proc. SPIE*, vol. 238, pp. 361-369, 1980.
- [21] D. Fischer *et al.*, "On Fourier-Toeplitz methods for separable elliptic problems," *Math. Comput.*, vol. 28, no. 26, pp. 349-368, Apr. 1974.
- [22] E. Cutting, J. H. Kwok, and S. N. Mohan, "The Venus radar mapper (VRM) mission," presented at the AIAA 22nd Aerospace Sci. Meet., Reno, NV, Jan. 1984.
- [23] R. T. Frankot and R. Chellappa, "Application of a shape from shading technique to SAR imagery," in *Proc. IEEE Int. Geosci. Remote Sensing Symp.*, Ann Arbor, MI, May 1987, pp. 1323-1329.
- [24] M. S. Scivier, M. A. Fiddy, and R. E. Burge, "Estimating SAR phase from complex SAR imagery," *J. Phys. D: Appl. Phys.*, vol. 19, no. 3, pp. 357-362, Mar. 1986.
- [25] A. E. Ennos, "Speckle interferometry," in *Laser Speckle and Related Phenomena*, J. C. Dainty, Ed. Berlin: Springer-Verlag, 1975.



**Robert T. Frankot** (S'76-M'87) received the B.S.E.E. degree from California State University, Long Beach, in 1977 and M.S.E.E. and E.E.E. degrees from the University of Southern California, Los Angeles, in 1980 and 1983, respectively.

He is currently a Staff Engineer with the Advanced Programs Division of Hughes Radar Systems Group, El Segundo, CA, and is also a research assistant at the University of Southern California Signal and Image Processing Institute.

Since 1978, he has been with the Hughes Aircraft Company where he has been involved in various aspects of sensor system development including the system analysis, development of image analysis, and image processing algorithms, radar system modeling, circuit design, and system integration. From 1976 to 1977, he was employed by the United States Air Force Flight Test Center, Edwards AFB, CA. He is currently a Ph.D. Candidate at the University of Southern California. His research interests are in signal processing, image processing, machine vision, and radar.

Mr. Frankot is a member of Tau Beta Pi and Eta Kappa Nu. He was awarded the Hughes Masters, Engineer, and Ph.D. fellowships.



**Rama Chellappa** (S'79-M'81-SM'83) was born in Madras, India, and received the B.S. degree (honors) in electronics and communication engineering from the University of Madras in 1975, and M.S. degree (with distinction) in electrical communication engineering from the Indian Institute of Science in 1977, and the M.S. and Ph.D. degrees in electrical engineering from Purdue University, West Lafayette, IN, in 1978 and 1981, respectively.

During 1979-1981, he was a Faculty Research Assistant at the Computer Vision Laboratory, University of Maryland, College Park, MD. Since 1986, he has been an Associate Professor in the Department of Electrical Engineering—Systems, University of Southern California, Los Angeles. His current research interests are in Signal and Image Processing, Computer Vision, and Pattern Recognition.

Dr. Chellappa is a member of Tau Beta Pi and Eta Kappa Nu. He is a coeditor of two volumes of selected papers on image analysis and processing, published in Fall 1985, and an Associate Editor for IEEE TRANSACTIONS ON ACOUSTICS, SPEECH AND SIGNAL PROCESSING. He was a recipient of a National Scholarship from the Government of India during 1969-1975. He received the 1975 Jawaharlal Nehru Memorial Award from the Department of Education, Government of India, the 1985 Presidential Young Investigator Award, and the 1985 IBM Faculty Development Award.